https://doi.org/10.1016/j.carbon.2021.02.003
This is the Pre-Published Version.

Rational design of microstructure and interphase enables high-capacity and long-life carbon anodes for potassium ion batteries

Hong Tan, Xiao qiong Du, Rui Zhou, Zhen Hou, Biao Zhang *

Department of Applied Physics, The Hong Kong Polytechnic University Kowloon, Hong Kong, China
*Corresponding author. E-mail: b3zhang@polyu.edu.hk

Abstract

Disordered carbon is considered as a potential anode material for potassium ion batteries (PIBs) due to its advantages in rate capability compared to graphite. Nevertheless, its capacity is usually limited below 300 mAh g^{-1}. Herein, we demonstrate the performance of low-cost pitch derived carbon could be significantly boosted through synergistic microstructure design and electrode/electrolyte interphase regulation. A considerable amount of mesopore is produced to provide the extra active sites for K ion storage and meanwhile, facilitate the charge transfer. The optimized carbon anode delivers a remarkable capacity of 460 mAh g^{-1} with outstanding rate capability up to 4.0 A g^{-1}. In-situ Raman spectra reveal the superb performance originates from K ion storage in both the mesopore and disordered graphene layers. The construction of a robust solid electrolyte interphase in ethylene glycol diethyl ether derived electrolyte further improves the long-term stability, leading to an exceptional capacity retention of 80% after 2000 cycles under a current density of 1.0 A g^{-1}. This strategy provides a facile approach to enhance the performance of carbon materials for PIBs via structure and interphase design.

Keywords:

Potassium ion battery, mesoporous carbon, solid electrolyte interphase, *in*-situ Raman

© 2021. This manuscript version is made available under the CC-BY-NC-ND 4.0 license http://creativecommons.org/licenses/by-nc-nd/4.0/.

1. Introduction

The 2020 *global renewables outlook report* predicts that around 55% of electricity generation will be shared by renewables like solar, wind and tides by 2050 to confront the depletion of fossil fuels and to meet the ever-growing energy demand in a green and sustainable way [1,2]. Meanwhile, the annual stationary storage of the intermittent energy forms will increase from 30 GWh in 2019 to 370 GWh in 2030 and to 3400 GWh in 2050 [1]. In this context, potassium-ion batteries (PIBs) emerge as a cost-effective choice for large scale energy storage bestowed by the abundance of potassium resources and similar working mechanisms with those of lithium-ion batteries (LIBs) [3,4]. Unlike sodium, potassium could form stable graphite intercalation compounds (GICs) KC_8 upon electrochemical intercalation into graphene galleries at below 0.3 V (vs. K^+/K), corresponding to a theoretical capacity of 279 mAh g^{-1} [5,6]. However, research on graphite and other SP^2-based carbon allotropes like graphene and expanded graphite as anodes for PIBs shows either a limited practical capacity of less than 250 mAh g^{-1} or sluggish kinetics [7–9]. Other insertion-type anode materials like $K_2Ti_6O_{13}$ and $KVPO_4F$ exhibit excellent rate capability but insufficient capacity [10,11]. Metallic Sb [12], Sn_4P_3 [13], and Bi [14] possess high reaction capacity with K, whereas the large volume expansion upon alloying raises concerns about long-term stability.

In search of appropriate anode materials for PIBs, disordered carbon appears as a promising candidate thanks to a large number of available precursors, low cost and facile manufacture methods [15]. In addition to the various intrinsic K ion storage sites, extra active sites could be readily incorporated into the carbon anode via heteroatom doping and pore generation [16,17]. For instance, N-doping has been proved an effective way to increase the capacity by providing additional defect sites [18,19]. S- [20] and P-doping [21,22] are capable of enlarging the d-spacing between graphene layers, thus allowing fast K ion migration. Along with the doping strategy, structure modifications such as introduction of pores, construction of hollow or yolk

shell structure, and particle size control are beneficial for the enhancement of material activities towards energy storage and catalysis by enlarging the electrochemical active areas [23–25]. Among those, building porous structure is an promising approach for enhancing anode performance. The merits are multifold. First, pore structures help improve the wettability of bulk carbon by shortening the electrode-electrolyte contacting distance. Second, the hollow structures could buffer the volume expansion upon exterior ion insertion [17,26]. Furthermore, mesopore plays a critical role in enhancing the capacity as more K ions could be adsorbed and stably stored in the relatively large cavities [27].

Herein, taking advantage of MgO particles with appropriate size [28], a facile and scalable MgO-templated method was adopted in this work to boost the capacity of disordered carbon by building mesoporous structures in the carbon skeletons. Mesophase pitch is chosen as the carbon precursors on the basis of its low cost and high carbon yield of over 80%. Besides, the electrode-electrolyte interphase was modified by shifting from the traditional carbonate-based electrolyte to an ether-based one. Compositional information of the as-formed solid electrolyte interphase (SEI) was confirmed by surface XPS analysis. Furthermore, K ions storage mechanisms in mesoporous carbon were investigated by *in*-situ Raman spectroscopy.

2. Experimental

2.1. Preparation of mesoporous carbon

For the synthesis of mesoporous carbon, mesophase pitch was firstly grind-mixed with magnesium acetate (Sigma Aldrich. Co) with a weight ratio of 1:5 in an agate mortar. Afterward, the grey-colored mixture was annealed at 800 ℃ for 2 h in a tube furnace with a ramp rate of 5 ℃ min^{-1} under Ar protection. Specifically, the chamber temperature was kept at 400 ℃ for 0.5h before rising to 800 ℃ to allow the full growth of MgO templates through the decomposition of magnesium acetate. The annealed black sample was then washed with excessive diluted HCl (7%) solution followed by deionized water to remove the residual MgO

and neutralize the sample. Finally, mesoporous carbon was obtained by drying the washed powder in a vacuum glass oven at 100 ℃ for 24h. For comparison, the unmodified carbon was prepared by directly carbonization at 800 ℃ for 2h after stabilizing the raw precursors at 300 ℃ for 4h in a muffle furnace. Accordingly, the carbon sample prepared with and without MgO template is marked as P-MgO and Neat-P, respectively.

2.2. Materials Characterizations

The morphology of the as-prepared carbon materials was characterized by scanning electron microscopy (Field-emission SEM, TESCAN MAIA3) and transmission electron microscopy (TEM, JEOL 2010F). Pore structure analysis was carried out via N_2 adsorption/desorption isotherms collected on a micromeritics ASAP 2020 machine. The surface compositional was examined via X-ray photoelectron spectroscopy (XPS) performed on a Nexsa X-ray Photoelectron Spectrometer system (Thermo Fisher Scientific Inc.) with monochromatic Al Kα radiation. Prior to the experiment, the cycled electrodes for XPS characterization were washed with the corresponding solvents to eliminate the residual salts. After drying in the glovebox, the electrodes were directly attached to a vacuum transfer chamber for the test. Raman spectra were collected using a Witec-Confocal Raman system (UHTS 600 SMFC VIS) with a laser length of 532 nm. The X-ray diffraction (XRD) patterns were obtained on a Diffractometer (Rigaku Smart Lab 9kW) with Cu-Kα radiation (λ=1.54178Å).

2.3. Electrochemical measurement

To fabricate the electrodes, Neat-P or P-MgO was homogeneously mixed with carbon black and sodium alginate by a weight ratio of 8:1:1 in an agate mortar. Subsequently, deionized water was drip-added while continuous mixing to prepare the slurry, which was then blade-cast onto the copper foil to make the electrode tape. After drying at 60 ℃ overnight, discs with a diameter of 12 mm were cut from the tape to be used as the electrodes. Typically, each electrode has an active mass of 0.8-1.2 mg. Standard CR2032 coin cells were assembled in a glove box

with O_2 and H_2O content below 0.5 ppm. The electrolytes were prepared by dissolving potassium bis(fluorosulfonyl)imide (KFSI, Energy chemical.) into ethylene glycol diethyl ether (EGDE, Macklin) or ethylene carbonate (EC, DoDoChem)/diethyl carbonate (DEC, DoDoChem) (1/1 by weight) via magnetic stirring for 12h in a glove box. One piece of Whatman (GF/D) glass fiber was used as the separator and potassium plate was adopted as both the counter and reference electrodes. For the full cell test, the cathode was made of $Fe_4(Fe(CN)_6)_3$ active materials and the slurry was coated on an aluminum foil following the same procedure in carbon electrode fabrication.

Galvanostatic tests were performed on LAND CT2001A Battery Testing systems within 0-3.0 V (vs. K^+/K). The cyclic voltammetry (CV) data were collected on an electrochemical workstation (Solartron Analytical 1400 cell test system) within the same voltage window at sweep rates varying from 0.2, 0.5, 1.0, 2.0 to 4.0 $mV \cdot s^{-1}$. The electrochemical impedance spectroscopy (EIS) was carried out on an SP150 workstation (Biologic, France). The galvanostatic intermittent titration technique (GITT) tests were conducted on Arbin battery systems.

3. Results and discussion

3.1 Mesopore-enhanced capacity and rate performance

The morphology of the as-fabricated carbon is first examined by SEM. It presents irregular bulk-shape particles for Neat-P, as shown in Fig. S1a. In comparison, P-MgO distinctively exhibits hollow structures with a large number of obvious macropores (Fig. S1b-d) and mesopores (Fig. S2). The successful incorporation of uniformly-distributed pores into the neat carbon matrix is further confirmed by TEM images of Neat-P (Fig. 1a-c) and P-MgO (Fig. 1d-f), in which typical positions of pores are marked by dashed lines and arrows. To examine the pore evolution in P-MgO, the BET measurement was carried out on both samples. As shown in Fig. S3, the N_2 adsorption/de-sorption curve for Neat-P shows fairly limited adsorbed quantity,

while that for P-MgO could be ascribed to the type IV isotherm [29], which typically results from the capillary condensation effect of mesopores. Accordingly, the directly annealed disordered carbon possesses scarcely any pores with a pore volume of less than 0.01 cm^3 g^{-1} and a surface area of merely 3.5 m^2 g^{-1} by BET method (Fig. 1g). A sharp contrast is observed for P-MgO, which has a pore volume of 0.99 cm^3 g^{-1} and a specific surface area of 333.2 m^2 g^{-1}. Besides, the sizes of most pores range from 10 to 50 nm, yielding an average pore size of 11.9 nm (Fig. 1h). This is in good agreement with that detected in the HRTEM image (Fig. 1f), which shows a pore size of 10~12 nm. Raman spectra (Fig. S4a) give a similar I_D/I_G ratio of 0.99 and 0.97 for Neat-P and P-MgO, respectively, as a reflection of the presence of defects and poor crystallinity. This is also confirmed by the broad bump-shape peak shown in the XRD patterns of both samples (Fig. S4b).

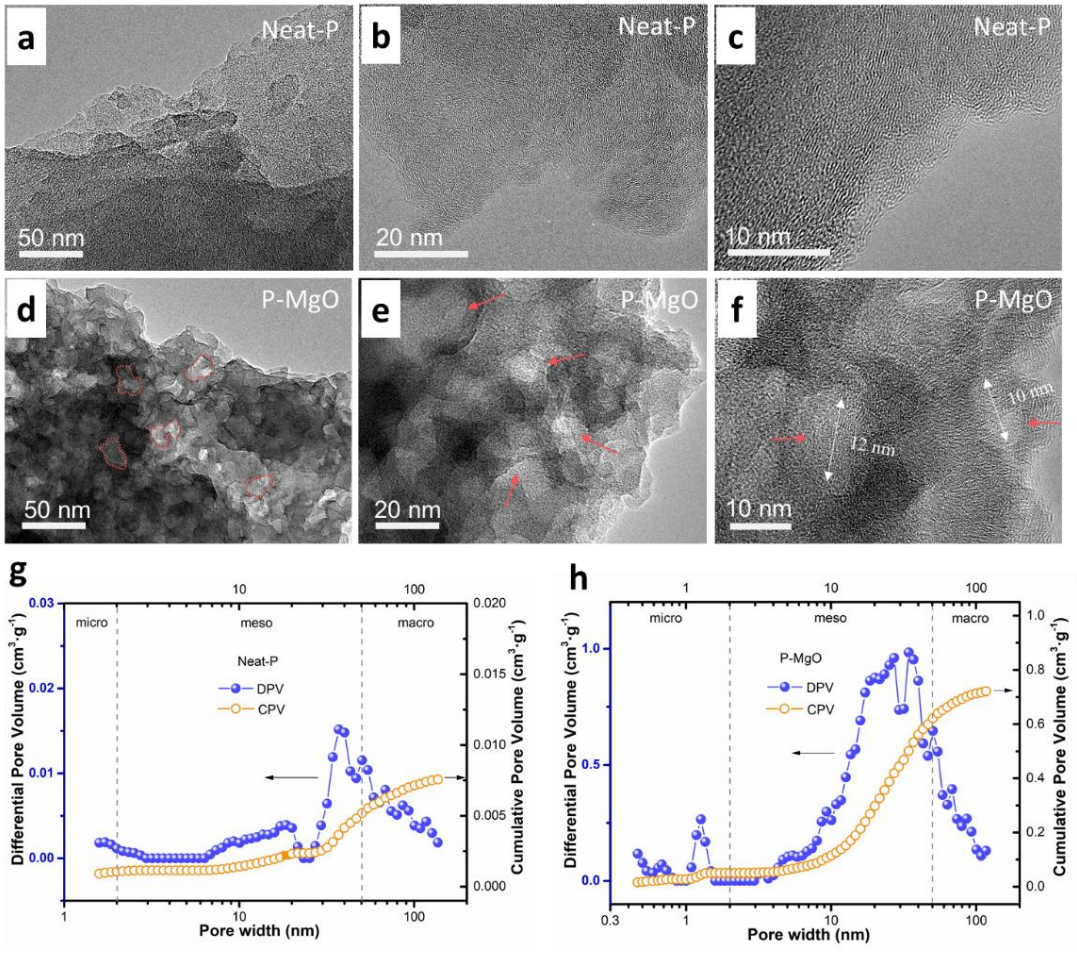

Fig. 1. TEM images of (a-c) Neat-P and (d-f) P-MgO and the corresponding pore size distribution results by BET method for (g) Neat-P and (h) P-MgO.

A galvanostatic rate test is then conducted to examine the effect of mesopores on the electrochemical performance of disordered carbon. Fig. 2a shows a capacity of 245 and 360 mAh g^{-1} at 0.05 A g^{-1} for Neat-P and P-MgO, respectively. Upon further increasing of the current density, a capacity of 290, 250, 206, 173, 146, and 110 mAh g^{-1} is obtained for the mesoporous carbon at 0.1, 0.2, 0.5, 1.0, 2.0, and 4.0 A g^{-1}, respectively. In contrast, when the current density increases to 0.2, 1.0 and 4.0 A g^{-1}, the capacity of Neat-P drops to 168, 99 and 30 mAh g^{-1}, respectively. As the current is set back to 0.1 and 0.05 A g^{-1}, the capacity for both samples could be resumed. The enhanced capacity should come from the increased K ion active sites in mesopores, as will be discussed later.

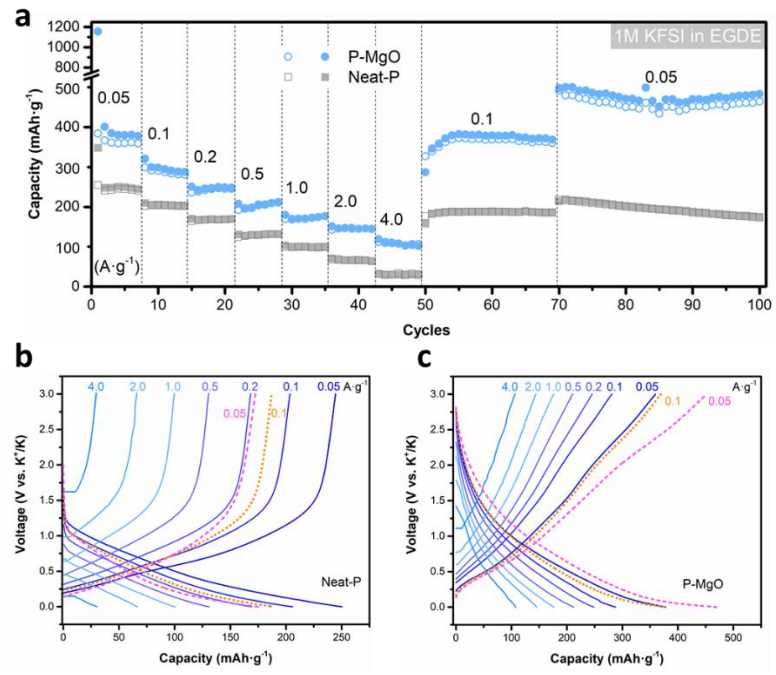

Fig. 2. (a) Rate performance of the as-prepared carbon and the corresponding voltage profiles for (b) Neat-P and (c) P-MgO under different rates. The dashed lines indicate the voltage profiles after recovery to low current rates.

The change of the dominant K ion storage mechanism is also reflected in the corresponding voltage profiles shown in Fig. 2b and 2c. It presents a plateau-slope combined charge-discharge profile for Neat-P with nearly no capacity delivered above 1.5 V. By contrast, a sheer slope-shaped profile is observed for P-MgO throughout 0-3.0 V without a clear plateau region.

Interestingly, the P-MgO electrode shows a nearly 100-mAh g^{-1} capacity increase after the recovery of current to 0.1 and 0.05 A g^{-1}, as indicated by the dashed lines in Fig. 2c. Such a phenomenon could arise from the activation process triggered by large current density [30]. The repeated intensive volume change opens up some enclosed cavities, thus allowing more K ions to flow into the carbon matrix. As a result, P-MgO exhibits a capacity as high as 460 mAh g^{-1} at 0.05 A g^{-1} after activation, which places it among the best of the state-of-the-art carbon-based anodes for PIBs, as illustrated in Fig. S5.

3.2 Interphase-boosted cycling stability

To explore the effect of electrode/electrolyte interphase on the long-term stability, the cyclic performance of P-MgO is also conducted in classic carbonate electrolyte, i.e., 1M KFSI in ECDEC. The cells using different electrolytes are examined at 1.0 A g^{-1} after pre-cycling at 0.1 A g^{-1} for ten cycles (Fig. 3a). They deliver similar capacities at the small current density, but large discrepancy is found at 1.0 A g^{-1}. A stable capacity of 223 and 159 mAh g^{-1} is obtained under EGDE- and ECDEC- based electrolyte, respectively, suggesting better rate capacity in the former electrolyte. Moreover, the cell with 1M KFSI/ECDEC starts to undergo frequent over-charging after the first 100 cycles, accompanying with the fluctuation of the Coulombic efficiency (indicated by the dashed circle). By contrast, the cell using 1M KFSI/EGDE exhibits a much stable cyclic performance. It shows a capacity of 178 mAh g^{-1} after 2000 cycles, corresponding to a capacity retention of 80%. Post-cycle investigation of the morphology of the electrodes reveals that the P-MgO anodes in both electrolytes remain intact after cycling (Fig. S6). The disparity between the performance of P-MgO anodes under the ether- and carbonate-based electrolytes may originate from the difference in the solid electrolyte interphase (SEI) formed.

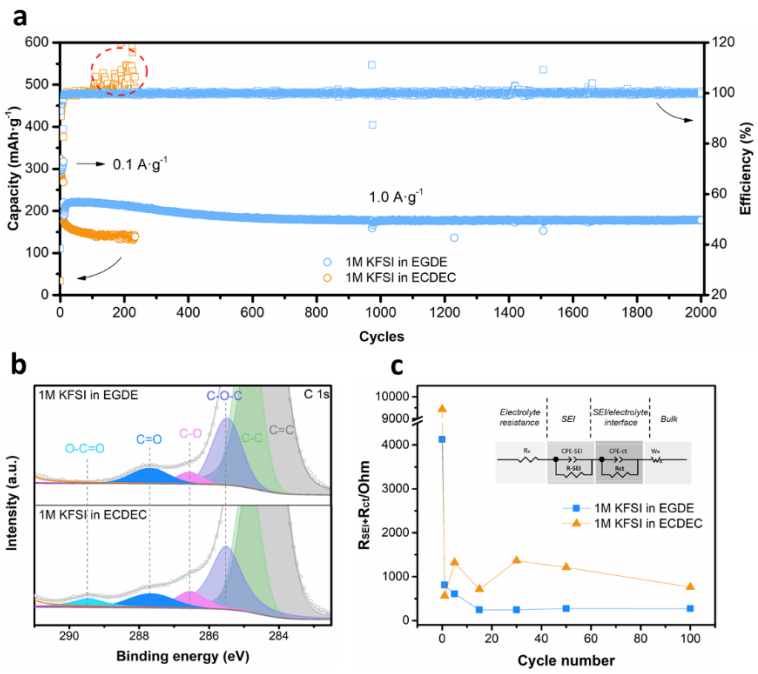

Fig. 3. (a) Cycling performance of P-MgO at 1.0 A g^{-1} and (b) C 1s surface XPS profiles of the electrodes after 3 cycles under 1M KFSI in EGDE and 1M KFSI in ECDEC; (c) Charge transfer resistance of the electrodes after different cycles.

XPS measurement was carried out on the electrodes after 3 cycles to investigate the surface composition. The full survey of both samples indicates that the surface layers mainly consist of C, O, K, F, S, N elements (Fig. S7). High-resolution C 1s peaks in Fig. 3b confirm the existence of sp^3 C-C, sp^2 C=C, C-O-C, C-O and C=O species for both electrolytes [14,31–34], whereas O-C=O species is only observable for the ECDEC-based electrolyte. In detail, the C-O, C=O and O-C=O species are mainly produced by the decomposition of the O-containing functional groups from the ether or carbonates, which leads to the formation of organic and inorganic compounds such as potassium-based oligomer $(CH_2CH_2\text{-}O\text{-})_nK$ (mainly from C-O) and alkyl carbonate RO-COOK (mainly from O-C=O) [35,36]. The possible decomposition mechanisms for EC, EGDE and KFSI are presented in the supporting information. The O 1s peaks in Fig. S8 also confirm the formation of RO-COOK and O-C-O species [36]. The presence of a large number of inorganic species in the organic matrix would decrease the SEI's flexibility [37], leading to the fracture of the SEI formed in ECDEC. The speculation is evidenced by the

fluctuation of Coulombic efficiency resulting from the repeated failure and re-construction. In comparison, the robust SEI derived in EGDE electrolyte essentially improve the stability for long-term cycles.

The SEI also has an important impact on the resistance on/through the surface of electrodes. To compare the values in the above two electrolytes, the EIS measurement is performed on the cells at various states, i.e., prior to cycle and after certain cycles. The original data are fitted using the model presented in the inset of Fig. 3c, which includes the high-frequency-responded processes at SEI film (R_{SEI}, except for pre-cycle state), medium-frequency-responded charge transfer at the interface of electrodes and electrolyte (R_{ct}), and low-frequency-related Warburg impedance of the bulk particle [38]. The summed value of R_{SEI} and R_{ct} for both electrolytes experience an abrupt decline (Fig. 3c, Fig. S9 and Table. S1, S2) owing to the gradual wetting of the electrodes. Upon further cycling, the resistance for EGDE slowly reduces to 250 Ω and maintains almost constant till 100 cycles thanks to the formation of a stable interface. In contrast to it, the value in ECDEC presents an averagely 5-fold higher value throughout the cycling process with oscillations in the value of R_{SEI} and R_{ct}.

3.3 Mesopore-related K ion storage mechanism

It remains unclear how K ions are stored in the mesoporous carbon. The CV rate sweeping test of P-MgO is adopted to probe the K ions behaviors based on the current division method proposed by Dunn et al. [39]. According to formula (1) and (2), where *i* refers to the current observed and *v* corresponds to the scanning rate. The overall current *i* consists of the capacitive-related k_1v and the diffusion-derived $k_2v^{1/2}$. After dividing formula (1) by $v^{1/2}$ into both sides, formula (2) is obtained for determining the k_1 and k_2 in $i(V)/v^{1/2}$ versus $v^{1/2}$ plot.

$$i=k_1v + k_2v^{1/2} \text{——} (1)$$

$$i(V)/v^{1/2} =k_1v^{1/2} + k_2 \text{——} (2)$$

The CV scanning curves and linear fitting results are presented in Fig. S10. It shows that the capacitive-controlled behaviors contribute 44%, 52%, 59%, 67% and 78% to the overall

capacity under the scan rate of 0.2, 0.5, 1.0, 2.0 and 4.0 mV s^{-1} (Fig. 4a, 4b). The large proportion of the capacitive contribution mainly results from the mesopore adsorption of K ions, while the residual capacity could be attributed to the K ions storage in expanded graphene layers or by adsorption on isolated/edge graphene layers [16]. As the capacitive behavior possesses fast kinetics, its contribution increases with the scan rates.

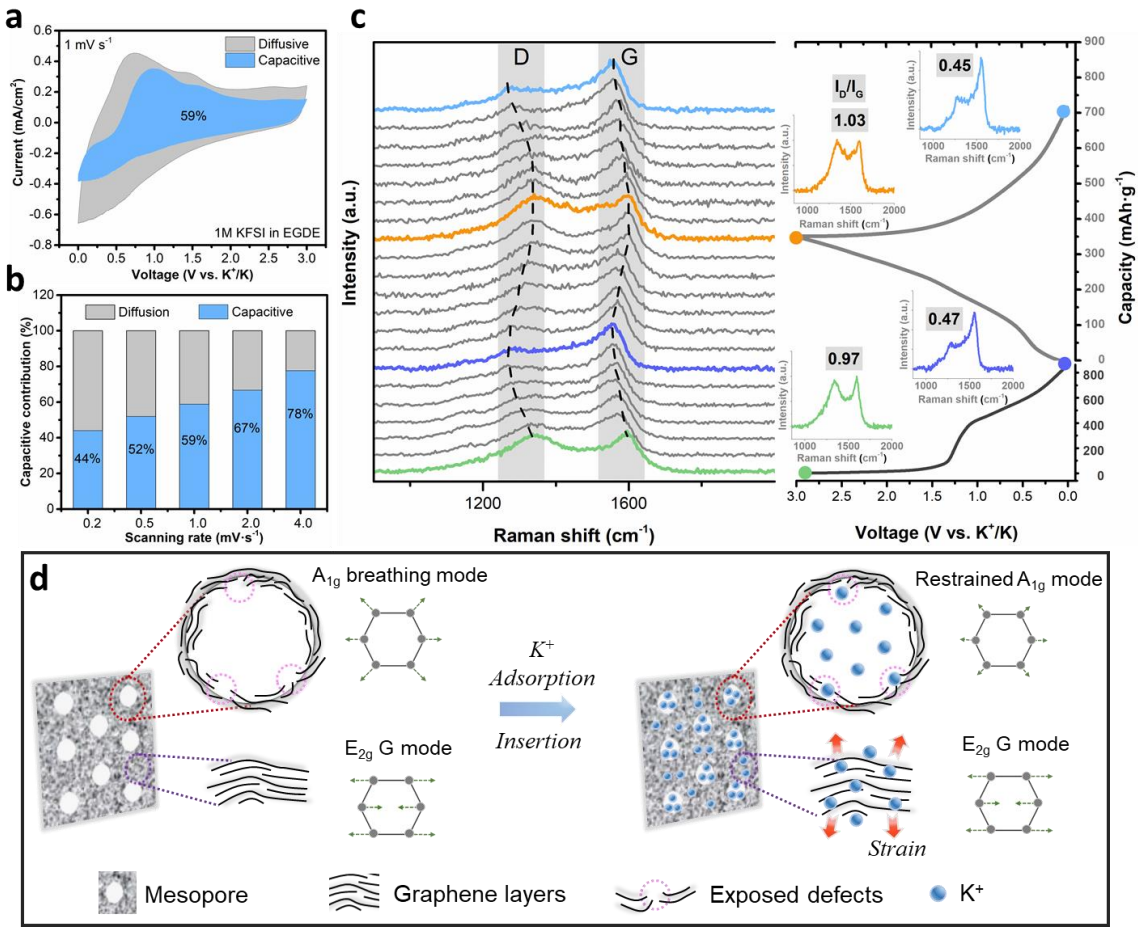

Fig. 4. (a) CV curve of P-MgO in 1M KFSI in EGDE with the blue-shadowed area indicating the capacitive-related region and (b) the capacitive contribution at various rates; (c) *In*-situ Raman spectra (left) collected upon the 1st charge/discharge and the 2nd discharge process (right); (d) Schematic illustration of the K storage mechanisms in mesoporous carbon.

To closely monitor the mesopore-related K storage mode, *in*-situ Raman spectra of neat P-MgO powders are real-time collected during the 1st discharge/charge and 2nd discharge processes under an *in*-situ Raman cell. As shown in Fig. 4c, prior to initial discharge, D-band and G-band appear at 1336 and 1595 cm^{-1}, which gradually shift to 1279 and 1558 cm^{-1},

respectively, when it is discharged to 0 V. Meanwhile, the slow weakening of D-band is observed, leading to the reduction of I_D/I_G ratio from 0.97 to 0.47 at 0 V. Upon further charging, both D- and G-band blue-shift back to 1337 and 1595 cm^{-1} along with the regaining of D-band intensity. Further recording of Raman spectra at 2^{nd} discharge reveals that this evolution is a highly reversible process. The red/blue shift of G-band during the discharge/charge process is ascribed to the adding/releasing of internal strain induced by the change of C-C bond length inside graphene layers [40,41]. In terms of the D-band, its position and intensity are varied simultaneously as the charge state changes. The defect-relating aromatic cluster from the amorphous component is electronically and vibrationally associated with the graphene lattice [42]. Therefore, its state could be affected by the strain inside the graphene layer during K ion insertion, resulting in the coincidental shift of D- and G- bands. The K ions storage mechanism in mesoporous carbon is schematically illustrated in Fig. 4d. The introduction of mesopores into the amorphous carbon matrix will make a large number of defects, such as graphene edges and voids, that are exposed to the cavities. Such defects could act as potential active sites for K ion storage and contribute a significant ratio to the signal of D-band, which stems from the A_{1g} breathing mode. Besides, the turbostratic carbon structure in the bulk part could store K ions by adsorption and insertion, which is correlated with the G-band following the E_{2g} mode. When K ions take occupation of the aforementioned sites, those defect-related vibrations become inactive, resulting in the restriction of the A_{1g} breathing mode and hence the weakening of D-peak [42]. Aside from defects, the meso-sized (2~50 nm) cavities also can effectively accommodate the K ions, contributing to the increase of the overall capacity. On the other hand, K ions insertion into graphene layers does not weaken the E_{2g} vibration mode. Instead, the induced strain arising from the expansion of graphene layers leads to the shift of G-band.

3.4 Full cell evaluation

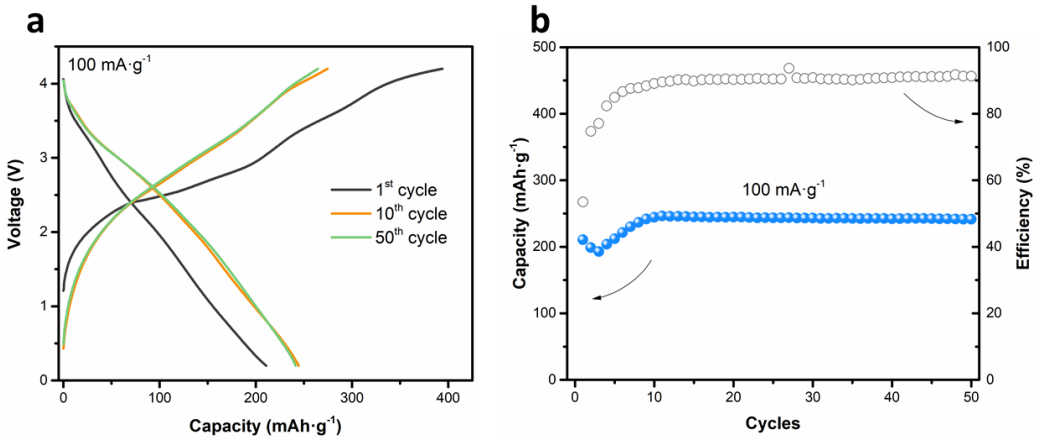

Fig. 5. (a) Voltage profiles of the as-assembled full cell adopting Prussian blue analog $K_xFe_4[Fe(CN)_6]_y$ as cathode and P-MgO as anode within 0.2-4.2 V; (b) the corresponding cycling performance at 100 mA g^{-1}.

As a proof of concept, a full cell is assembled with Prussian blue analog $Fe_4(Fe(CN)_6)_3$ cathode and P-MgO anode using 1M KFSI in EGDE as an electrolyte. $Fe_4(Fe(CN)_6)_3$ was synthesized based on a previous report [43], which gives a highly crystallized structure, as indicated by the XRD pattern (Fig. S11a). The cathode delivers a reversible capacity of 77.8 mAh g^{-1} (Fig. S11b) with an average potential of 3.3 V. Since the pristine material is K-ion deficient, a pre-cycle process in half cells is required to prepare the $K_xFe_4[Fe(CN)_6]_y$ for acting as the cathode in the full cell. To eliminate the SEI-related irreversibility, the P-MgO electrode is charged/discharged for three cycles in a half cell before assembling the full cell. Coupling with the $K_xFe_4(Fe(CN)_6)_3$, a 2.5-V class PIB is obtained (Fig. 5a). The cell delivers a stable capacity of around 245 mAh g^{-1} (based on the mass of anode) and shows no apparent decay after 50 cycles (Fig. 5b), indicating the compatibility of the developed mesoporous carbon anode with the cathode for future application. For comparison, a $K_xFe_4[Fe(CN)_6]_y$/Neat-P full cell is also assembled following the same procedure, which delivers a lower capacity of around 102 mAh g^{-1} (based on the mass of anode) and decays to 80 mAh g^{-1} after 50 cycles (Fig. S12).

4. Conclusions

In summary, a mesoporous carbon is fabricated via a facile MgO-templated method from high-carbon-yield and low-cost pitch. Compared to the directly annealed disordered carbon, the capacity is considerably increased from 245 to 360 mAh g^{-1} at 0.05 A g^{-1}, which could be further enhanced to 460 mAh g^{-1} via large current activation. Moreover, the as-prepared mesoporous carbon shows a decent rate capability with a capacity of 110 mAh g^{-1} at 4.0 A g^{-1} and proves an ultra-stable cyclic performance with a capacity of 178 mAh g^{-1} after 2000 cycles at 1.0 A g^{-1} using 1M KFSI in EGDE electrolyte. This outstanding performance, on the one hand, originates from the mesopore incorporation, which provides plenty of K ion storage active sites. On the other hand, the formation of a robust SEI in ether-based electrolyte significantly boost long-term stability. The charge storage mechanism is revealed by the CV rate sweep method and *in*-situ Raman spectroscopy. This work provides a simple way of enhancing the overall electrochemical performance of neat carbon via structure and interphase modification, which helps promote the application of carbon anode for PIBs.

Acknowledgements

This work is supported by the Hong Kong Research Grants Council through the Early Career Scheme (Project No. 25215918).

References

[1] IRENA, Global Renewables Outlook: Energy transformation 2050, 2020.

[2] D. Larcher, J.M. Tarascon, Towards greener and more sustainable batteries for electrical energy storage, Nat. Chem. 7 (2015) 19–29.

[3] H. Kim, J.C. Kim, M. Bianchini, D.H. Seo, J. Rodriguez-Garcia, G. Ceder, Recent Progress and Perspective in Electrode Materials for K-Ion Batteries, Adv. Energy Mater. 8 (2018) 1–19.

[4] W. Zhang, Y. Liu, Z. Guo, Approaching high-performance potassium-ion batteries via advanced design strategies and engineering, Sci. Adv. 5 (2019) 1–14.

[5] J. Zhao, X. Zou, Y. Zhu, Y. Xu, C. Wang, Electrochemical Intercalation of Potassium into Graphite, Adv. Funct. Mater. 26 (2016) 8103–8110.

[6] L. Wang, J. Yang, J. Li, T. Chen, S. Chen, Z. Wu, J. Qiu, B. Wang, P. Gao, X. Niu, H. Li, Graphite as a potassium ion battery anode in carbonate-based electrolyte and ether-based electrolyte, J. Power Sources. 409 (2019) 24–30.

[7] Z. Jian, W. Luo, X. Ji, Carbon Electrodes for K-Ion Batteries, J. Am. Chem. Soc. 137 (2015) 11566–11569.

[8] W. Luo, J. Wan, B. Ozdemir, W. Bao, Y. Chen, J. Dai, H. Lin, Y. Xu, F. Gu, V. Barone, L. Hu, Potassium Ion Batteries with Graphitic Materials, Nano Lett. 15 (2015) 7671–7677.

[9] Y. An, H. Fei, G. Zeng, L. Ci, B. Xi, S. Xiong, J. Feng, Commercial expanded graphite as a low–cost, long-cycling life anode for potassium–ion batteries with conventional carbonate electrolyte, J. Power Sources. 378 (2018) 66–72.

[10] S. Dong, Z. Li, Z. Xing, X. Wu, X. Ji, X. Zhang, Novel Potassium-Ion Hybrid Capacitor Based on an Anode of $K_2Ti_6O_{13}$ Microscaffolds, ACS Appl. Mater. Interfaces. 10 (2018) 15542–15547.

[11] H. Tan, X. Du, J.Q. Huang, B. Zhang, $KVPO_4F$ as a novel insertion-type anode for potassium ion batteries, Chem. Commun. 55 (2019) 11311–11314.

[12] J. Zheng, Y. Yang, X. Fan, G. Ji, X. Ji, H. Wang, S. Hou, M.R. Zachariah, C. Wang, Extremely stable antimony-carbon composite anodes for potassium-ion batteries, Energy Environ. Sci. 12 (2019) 615–623.

[13] W. Zhang, W.K. Pang, V. Sencadas, Z. Guo, Understanding High-Energy-Density Sn_4P_3 Anodes for Potassium-Ion Batteries, Joule. 2 (2018) 1534–1547.

[14] J. Huang, X. Lin, H. Tan, B. Zhang, Bismuth Microparticles as Advanced Anodes for

Potassium-Ion Battery, Adv. Energy Mater. 8 (2018) 1–7.

[15] R.A. Adams, A. Varma, V.G. Pol, Carbon Anodes for Nonaqueous Alkali Metal-Ion Batteries and Their Thermal Safety Aspects, Adv. Energy Mater. 9 (2019).

[16] X. Lin, J. Huang, B. Zhang, Correlation between the microstructure of carbon materials and their potassium ion storage performance, Carbon N. Y. 143 (2019) 138–146.

[17] Y. Wu, H. Zhao, Z. Wu, L. Yue, J. Liang, Q. Liu, Y. Luo, S. Gao, S. Lu, G. Chen, X. Shi, B. Zhong, X. Guo, X. Sun, Rational design of carbon materials as anodes for potassium-ion batteries, Energy Storage Mater. 34 (2021) 483–507.

[18] X. Chang, X. Zhou, X. Ou, C.S. Lee, J. Zhou, Y. Tang, Ultrahigh Nitrogen Doping of Carbon Nanosheets for High Capacity and Long Cycling Potassium Ion Storage, Adv. Energy Mater. 9 (2019) 1–7.

[19] D. Li, X. Ren, Q. Ai, Q. Sun, L. Zhu, Y. Liu, Z. Liang, R. Peng, P. Si, J. Lou, J. Feng, L. Ci, Facile Fabrication of Nitrogen-Doped Porous Carbon as Superior Anode Material for Potassium-Ion Batteries, Adv. Energy Mater. 8 (2018) 1–9.

[20] M. Chen, W. Wang, X. Liang, S. Gong, J. Liu, Q. Wang, S. Guo, H. Yang, Sulfur/Oxygen Codoped Porous Hard Carbon Microspheres for High-Performance Potassium-Ion Batteries, Adv. Energy Mater. 8 (2018) 1–9.

[21] Y. Qian, S. Jiang, Y. Li, Z. Yi, J. Zhou, T. Li, Y. Han, Y. Wang, J. Tian, N. Lin, Y. Qian, In Situ Revealing the Electroactivity of P-O and P-C Bonds in Hard Carbon for High-Capacity and Long-Life Li/K-Ion Batteries, Adv. Energy Mater. 9 (2019) 1–10.

[22] J. Chen, Y. Cheng, Q. Zhang, C. Luo, H. Li, Y. Wu, H. Zhang, X. Wang, H. Liu, X. He, J. Han, D. Peng, M. Liu, M. Wang, Designing and Understanding the Superior Potassium Storage Performance of Nitrogen/Phosphorus Co-Doped Hollow Porous Bowl-Like Carbon Anodes, 2007158 (2020) 1–12.

[23] W. Jiao, C. Chen, W. You, X. Zhao, J. Zhang, Y. Feng, P. Wang, R. Che, Hollow Palladium-Gold Nanochains with Periodic Concave Structures as Superior ORR

Electrocatalysts and Highly Efficient SERS Substrates, Adv. Energy Mater. 10 (2020) 1–13.

[24] W. Jiao, C. Chen, W. You, J. Zhang, J. Liu, R. Che, Yolk–Shell Fe/Fe_4N@Pd/C Magnetic Nanocomposite as an Efficient Recyclable ORR Electrocatalyst and SERS Substrate, Small. 15 (2019) 1–13.

[25] L. Yang, X. Zhu, X. Li, X. Zhao, K. Pei, W. You, X. Li, Y. Chen, C. Lin, R. Che, Conductive Copper Niobate: Superior Li^+-Storage Capability and Novel Li^+-Transport Mechanism, Adv. Energy Mater. 9 (2019) 1–10.

[26] Q. Li, Y. Zhao, H. Liu, P. Xu, L. Yang, K. Pei, Q. Zeng, Y. Feng, P. Wang, R. Che, Dandelion-like Mn/Ni co-doped CoO/C hollow microspheres with oxygen vacancies for advanced lithium storage, ACS Nano. 13 (2019) 11921–11934.

[27] Y. Qian, S. Jiang, Y. Li, Z. Yi, J. Zhou, J. Tian, N. Lin, Y. Qian, Understanding mesopore volume-enhanced extra-capacity: Optimizing mesoporous carbon for high-rate and long-life potassium-storage, Energy Storage Mater. 29 (2020) 341–349.

[28] C. Liang, Z. Li, S. Dai, Mesoporous carbon materials: Synthesis and modification, Angew. Chemie - Int. Ed. 47 (2008) 3696–3717.

[29] K.S.W. Sing, Reporting physisorption data for gas/solid systems with special reference to the determination of surface area and porosity (Recommendations 1984), Pure Appl. Chem. 57 (1985) 603–619.

[30] K. Bachtin, D. Kramer, V.S.K. Chakravadhanula, X. Mu, V. Trouillet, M. Kaus, S. Indris, H. Ehrenberg, C. Roth, Activation and degradation of electrospun $LiFePO_4$ battery cathodes, J. Power Sources. 396 (2018) 386–394.

[31] S. Dapoz, N. Betz, M.-J. Guittet, A. Le Moël, ESCA characterization of heparin-like fluoropolymers obtained by functionalization after grafting induced by swift heavy ion irradiation, Nucl. Instruments Methods Phys. Res. Sect. B Beam Interact. with Mater. Atoms. 105 (1995) 120–125.

[32] D. Briggs, G. Beamson, Primary and secondary oxygen-induced C1s binding energy shifts in x-ray photoelectron spectroscopy of polymers, Anal. Chem. 64 (1992) 1729–1736.

[33] F. Bournel, C. Laffon, P. Parent, G. Tourillon, Adsorption of some substituted ethylene molecules on Pt (111) at 95 K Part 1: NEXAFS, XPS and UPS studies, Surf. Sci. 350 (1996) 60–78.

[34] W.E. Morgan, J.R. Van Wazer, W.J. Stec, Inner-orbital photoelectron spectroscopy of the alkali metal halides, perchlorates, phosphates, and pyrophosphates, J. Am. Chem. Soc. 95 (1973) 751–755.

[35] X. Ren, X. Zhang, Z. Shadike, L. Zou, H. Jia, X. Cao, M.H. Engelhard, B.E. Matthews, C. Wang, B.W. Arey, X. Yang, J. Liu, J. Zhang, W. Xu, Designing Advanced In Situ Electrode/Electrolyte Interphases for Wide Temperature Operation of 4.5 V Li||$LiCoO_2$ Batteries , Adv. Mater. 2004898 (2020) 2004898.

[36] L. Fan, S. Chen, R. Ma, J. Wang, L. Wang, Q. Zhang, E. Zhang, Z. Liu, B. Lu, Ultrastable Potassium Storage Performance Realized by Highly Effective Solid Electrolyte Interphase Layer, Small. 14 (2018) 1–8.

[37] J. Huang, X. Guo, X. Du, X. Lin, J.Q. Huang, H. Tan, Y. Zhu, B. Zhang, Nanostructures of solid electrolyte interphases and their consequences for microsized Sn anodes in sodium ion batteries, Energy Environ. Sci. 12 (2019) 1550–1557.

[38] G. Assat, C. Delacourt, D.A. Dalla Corte, J.-M. Tarascon, Practical assessment of anionic redox in Li-rich layered oxide cathodes: a mixed blessing for high energy Li-ion batteries, J. Electrochem. Soc. 163 (2016) A2965.

[39] J. Wang, J. Polleux, J. Lim, B. Dunn, Pseudocapacitive contributions to electrochemical energy storage in TiO_2(anatase) nanoparticles, J. Phys. Chem. C. 111 (2007) 14925–14931.

[40] J.C. Chacon-torres, L. Wirtz, T. Pichler, Manifestation of Charged and Strained

Graphene Layers in the Raman Response of Graphite Intercalation Compounds Manifestation of Charged and Strained Graphene Layers in the Raman Response of Graphite Intercalation Compounds, (2013) 9249–9259.

[41] J.C. Chacón-Torres, L. Wirtz, T. Pichler, Raman spectroscopy of graphite intercalation compounds: Charge transfer, strain, and electron-phonon coupling in graphene layers, Phys. Status Solidi Basic Res. 251 (2014) 2337–2355.

[42] A. Ferrari, J. Robertson, Interpretation of Raman spectra of disordered and amorphous carbon, Phys. Rev. B - Condens. Matter Mater. Phys. 61 (2000) 14095–14107.

[43] C. Zhang, Y. Xu, M. Zhou, L. Liang, H. Dong, M. Wu, Y. Yang, Y. Lei, Potassium Prussian Blue Nanoparticles: A Low-Cost Cathode Material for Potassium-Ion Batteries, Adv. Funct. Mater. 27 (2017).